

Fine-grained nickel deformed by direct impact at different velocities: Microstructure and mechanical properties

G. Dirras^{a,*}, H. Couque^b, J. Gubicza^c, A. Ouarem^a, T. Chauveau^a, P. Jenei^c

^a LPMTM, CNRS UPR 9001, Université Paris 13, 99 Avenue Jean Baptiste Clément, 93430 Villetaneuse, France

^b Nexter-Munitions, 7 route de Guerry, 18023 Bourges Cedex, France

^c Department of Materials Physics, Eötvös Loránd University, P.O.B. 32, H-1518, Budapest, Hungary

ARTICLE INFO

Article history:

Received 9 January 2010

Received in revised form 4 March 2010

Accepted 11 March 2010

Keywords:

Nickel
Dynamic strain
Impact
Microstructure
Recrystallization

ABSTRACT

High purity electrolytic nickel (99.99%) samples deformed dynamically in compression using a direct impact Hopkinson pressure bar test at the velocities of 10.9, 28.2 and 70.6 m s⁻¹ were investigated. The dislocation density increased with increasing the impact velocity up to 28.2 m s⁻¹ resulting in an increase of nanohardness and quasi-static compressive flow stress. At the same time, a decrease of the fraction of $\Sigma 3$ coincident site lattice boundaries was observed for the benefit of $\Sigma 1$ low angle grain boundaries having misorientations lower than 15°. Increasing the velocity to 70.6 m s⁻¹ led to a decrease of the dislocation density, in parallel with the regeneration of $\Sigma 3$ boundaries. As a consequence, the nanohardness decreased to a similar value as in the initial state. These observations suggest possible dynamic recovery/recrystallization that might have occurred at the highest impact velocity.

© 2010 Elsevier B.V. All rights reserved.

1. Introduction

For tailoring materials with enhanced properties, the “grain boundary engineering” concept, *i.e.* a manipulation of grain boundary structure via thermomechanical processes has been first stated by Watanabe [1] and a detailed overview has been provided by Randle [2]. In general, samples having higher fractions of structurally ordered “special” coincidence site lattice (CSL) boundaries exhibit improved properties. For instance, enhanced intergranular corrosion resistance due to the increase in the fractions of low Σ CSL type grain boundaries ($\Sigma \leq 29$) has been reported by Kim et al. [3] and Lin et al. [4].

As for the mechanical properties, it was found that the ductility of fine-grained materials, that is usually lower compared with their coarse-grained counterparts [5], can be improved by the increase of the fraction of high angle grain boundaries [6]. In the context of enhancing mechanical properties by boundary engineering, electrodeposition was successfully used to process nanostructured Cu [7,8] and Ni [9] with a large fraction of $\Sigma 3$ coherent twin boundaries that were believed to result in high strength and good ductility during quasi-static tensile tests. Indeed, in the absence of nanotwins, the reported high mechanical performances were dramatically reduced [10–12].

In fine-grained metallic materials having a mean grain size higher than several hundred of nanometers, the movement of dislocations controls the plastic deformation. It has been shown recently, that during quasi-static compression of ultrafine-grained Ni processed by powder metallurgy routes, the activity of dislocations destroyed, at least partially the $\Sigma 3$ boundaries existing in the as-processed material and led to a macroscopic softening [13,14]. This effect was particularly noticeable when large amplitude cyclic simple shear was applied on these sintered Ni materials [14]. These experimental observations suggest that beside the as-processed microstructure, the deformation conditions have also a significant effect on the mechanical performance of advanced engineering materials, therefore the influence of deformation mode, temperature and strain rate on the deformation mechanisms should also be studied.

The deformation mechanisms underlying the macroscopic mechanical behavior under quasi-static plasticity of conventional metallic materials such as Ni are well understood [15]. Nickel is one of the structural materials investigated and used in a wide range of applications, from nanodevices such as MEMS [12,16] to military applications (antiarmor systems). In the latter case, the material experiences high strain rate deformation, that could modify the as-processed microstructure by means of thermomechanical processes mostly due to the increase of temperature. Particularly dynamic recrystallization was reported to occur during extreme deformations in microstructure refinement procedures [17].

* Corresponding author. Tel.: +33 1 49 40 39 38.

E-mail address: dirras@univ-paris13.fr (G. Dirras).

Table 1
Chemical composition (in percent) of the as-received Ni material.

Ni	Co	Cu	Zn	Fe	P	C	S	Pb
Balance	0.0003	0.0010	0.0005	0.0030	0.0002	0.0050	0.0005	0.0001

In the present study, high purity electrolytic Ni samples containing a large fraction of $\Sigma 3$ boundaries in the as-processed state were submitted to high strain rate impact tests. The changes in the microstructure at different impact velocities and their influence on the subsequent mechanical behavior are investigated.

2. Experimental procedures

The chemical composition of the high purity (99.99%) electrolytic nickel material is given in Table 1. From the as-received square plates, cylinders of about 9.0 mm in diameter and 5.0 mm in height were prepared and subsequently dynamically deformed in compression using a direct Hopkinson pressure bar test [18]. The test consists in impacting at a constant velocity with a striker a specimen placed against a Hopkinson pressure bar. Tests were conducted at three impact velocities of 10.9, 28.2 and 70.6 m s⁻¹. The generated strain rates were in the regime of 10³–10⁴ s⁻¹. The dimensions of the samples before and after the impact tests and the calculated imposed strain values are summarized in Table 2.

For texture analysis and microstructure investigations, specimens were cut out from the impacted and the initial samples and subsequently electropolished in an A2 electrolytic solution at room temperature and a fixed voltage of 7V for 15 s, using a Tenupol® electropolishing apparatus from Struers.

X-ray diffraction experiments (XRD) for texture analysis were carried out on the impacted and the opposite faces of the samples, but both measurements gave the same result. To describe the results, a direct macroscopic reference system (ND, RD, and TD) has been attached on the analyzed faces (where ND is the normal direction, taken parallel to the impact direction, RD and TD are the rolling (longitudinal) and transverse directions, respectively, lying in the impacted surface). Texture data were collected using an Inel™ four-circles goniometer in Bragg–Brentano geometry with a point focus X-ray source having CoK α radiation ($\lambda = 0.17902$ nm). The measurement consisted first of the determination of the Bragg angles for the {1 1 1}, {2 0 0}, {2 2 0} reflections and then the acquisition of the corresponding pole figures. After corrections of the experimental pole figures (background, defocusing and normalization), the determination of the orientation distribution functions (ODF) was performed using Labotex® software [19].

X-ray line profile analysis was also conducted to investigate the microstructure of the samples in the initial state and after processing by the impact tests and after room temperature quasi-static compression of the initial and the impacted samples. The surface normal to the impact and quasi-static compression directions was studied for all materials. The X-ray line profiles were measured by high-resolution rotating anode diffractometer (Nonius, FR 591) using CuK α_1 radiation ($\lambda = 0.15406$ nm). Two-dimensional imaging plates detected the Debye–Scherrer diffraction rings. The line pro-

Table 2
Samples characteristics before and after the impact test. V_i is the impact velocity, D_0 is the initial diameter, D_f is the diameter after the impact, H_0 is the initial height, H_f is the final height, ϵ_{axial} is the axial deformation in the impact direction defined as $\epsilon = \ln(H_f/H_0)$.

V_i (m s ⁻¹)	D_0 (mm)	H_0 (mm)	D_f (mm)	H_f (mm)	ϵ_{axial}
10.9	9.0	5.0	9.86	4.34	0.141
28.2	9.0	5.0	12.89	2.48	0.701
70.6	9.0	5.0	19.5	0.53	2.244

files were determined as the intensity distribution perpendicular to the rings obtained by integrating the two-dimensional intensity distribution along the rings. The line profiles were evaluated by the extended convolutional multiple whole profile (eCMWP) analysis [20,21]. In this method, the experimental pattern is fitted by the convolution of the instrumental pattern and the theoretical size and strain line profiles. The theoretical profile functions used in this fitting procedure are calculated on the basis of a model of the microstructure, where the crystallites have spherical shape and log-normal size distribution, and the lattice strains are assumed to be caused by dislocations and twins. The mean crystallite size, the dislocation density (ρ_{dis}) and the twin fault probability (β) were obtained from the fitting. The latter quantity is defined as the relative fraction of twin boundaries among {1 1 1} lattice planes.

The microstructures before and after impact tests were also investigated by electron backscattering diffraction (EBSD) technique using a Zeiss Supra 40VP FEG scanning electron microscope (SEM). The EBSD scans covered regions of approximately 150 $\mu\text{m} \times 150 \mu\text{m}$ using a step size between neighboring measurement positions of 0.1 μm . The average grain size, the fraction of low angle grain boundaries (LAGBs), high angle grain boundaries (HAGBs) and specially $\Sigma 3$ boundaries were extracted from the EBSD scans by use of OIM software version 4 from TexSem Laboratories (TSL). The Σ boundaries were identified according to the Brandon criterion and the grain boundary fractions were expressed as proportion of the total boundary projected length in the map.

The mechanical behavior of the initial and impacted samples was studied by nanoindentation and by quasi-static compression tests at room temperature. Nanohardness measurements were carried out using an UMIS nanoindentation device with Berkovich indenter and applying a maximum load of 5 mN. The indentation rate was 0.15 mN s⁻¹. Four hundred indentations were carried out arranging the indents in a 20 \times 20 matrix. The distance between the neighboring indents was 20 μm . The hardness H is characterized by a number as [22]:

$$H = \frac{P_m}{24.5h_m^2}, \quad (1)$$

where P_m is the maximum load (5 mN) and h_m is the maximum penetration depth during indentation.

The quasi-static uniaxial compression tests for evaluating the macroscopic mechanical behavior were conducted at a strain rate of 10⁻⁴ s⁻¹ by means of a universal Instron testing machine (model 1195). For each compression test, the strain was evaluated from crosshead displacement corrected by the stiffness of the testing machine.

3. Results and discussion

3.1. EBSD investigations

Figs. 1 and 2 show the grain orientation map and the $\Sigma 3$ boundaries, respectively, for the initial sample and after impact test at different velocities. The evolution of the grain structure can be described as follows:

- (i) In the initial state (Figs. 1a and 2a), the microstructure consisted of equiaxed grains. The majority of grain boundaries, about 97%, are HAGBs (with misorientation across the boundary larger than 15°) including $\Sigma 3$ boundaries (with misorientation of about 60°), whose fraction is about 50%. The average grain size determined from the areas bounded by HAGBs in the EBSD images was about 3.9 μm .
- (ii) After the impact test at the velocity of 10.9 m s⁻¹ (Figs. 1b and 2b), some grains are elongated and the ori-

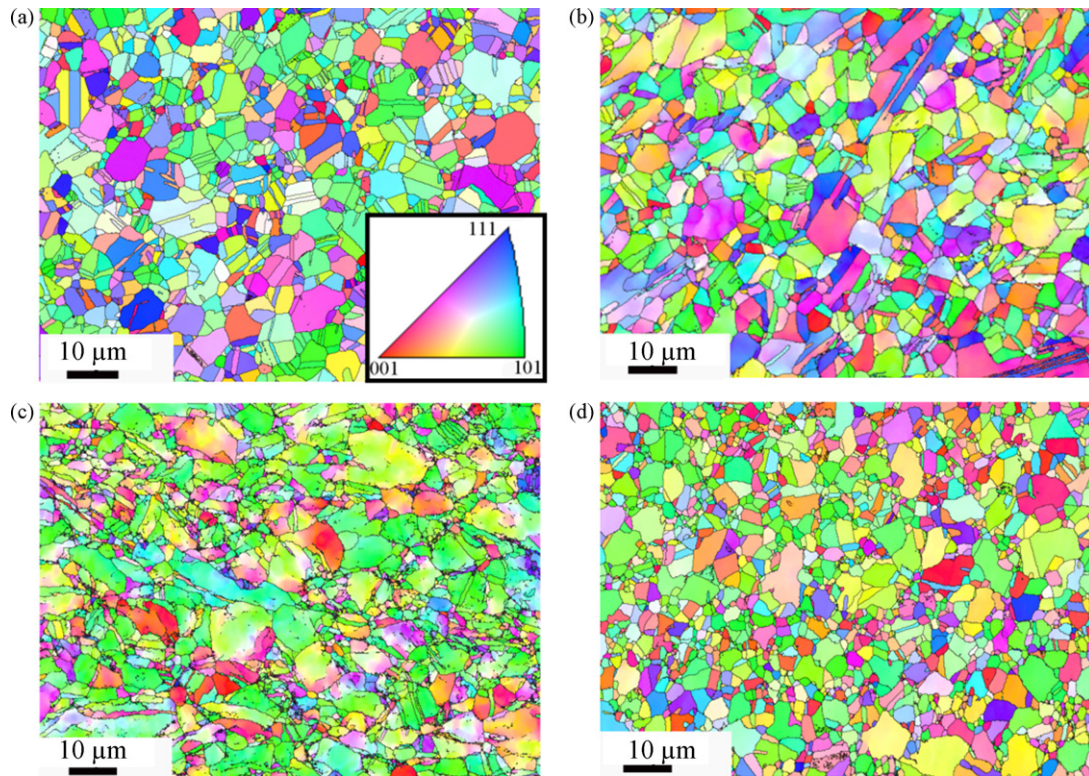


Fig. 1. EBSD images of investigated Ni samples. (a) Initial state; (b)–(d) after direct compression impacts at 10.9, 28.2 and 70.6 m s^{-1} velocities, respectively.

entation of most of the grains is changing as exemplified by gradual change of the color inside a given grain. In addition, the misorientation between grains increases as it can be seen from the standard stereographic projection inset in Fig. 1. These observations indicate that most probably subgrains

are formed inside the grains during impact test that may act as coherently scattering domains in X-ray diffraction experiments. This point is supported by the X-ray line profile analysis as it is discussed later. Comparing to the initial state, the fraction of the HAGBs dropped to 88% and that of $\Sigma 3$

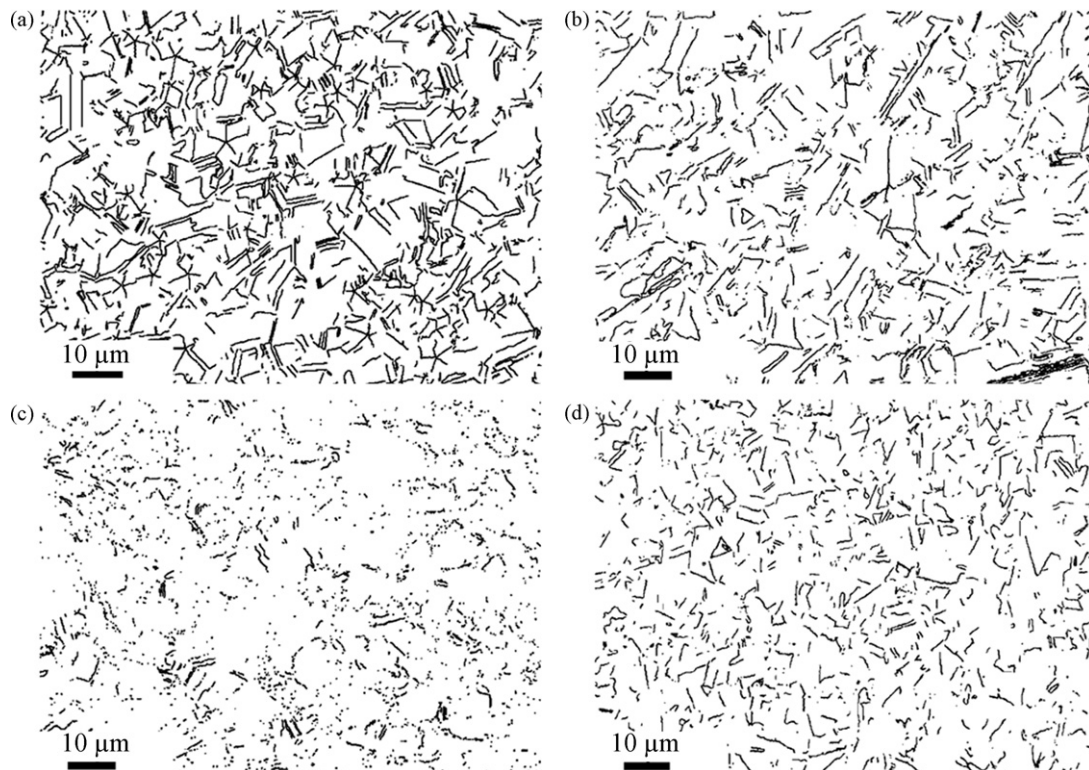


Fig. 2. Evolution of the $\Sigma 3$ boundary maps corresponding Fig. 1. (a) Initial state; (b)–(d) after direct compression impacts at 10.9, 28.2 and 70.6 m s^{-1} velocities, respectively.

boundaries to 33%. The average grain size determined from the area of grains bounded by HAGBs was about 4.5 μm . The increase of the grain size compared to the initial state might be apparent and associated with the decrease of the relative fraction of $\Sigma 3$ boundaries that initially divide grains into smaller areas, as it can be seen from Fig. 2b.

- (iii) In the case of the sample impacted at the velocity of 28.2 m s^{-1} (Figs. 1c and 2c), the HAGBs fraction sharply decreased to 57% and that of $\Sigma 3$ boundaries to about 7%. Indeed, it seems that within the $\Sigma 3$ boundaries, twin boundaries (TBs) were particularly affected by the impact test as only very few of them were observed in the EBSD scans (Fig. 2c). Accordingly, the average grain size determined from the area of grains bounded by HAGBs increased further to about 6 μm . In addition, Fig. 1c indicates a development of a strong crystallographic texture as it can be seen from the projection of the grain orientations in the ND direction illustrated by the standard stereographic projection inset.
- (iv) For the sample impacted at the highest velocity of 70.6 m s^{-1} , the microstructure was qualitatively similar to that of the initial state (see Figs. 1d and 2d). The HAGBs fraction increased back to 92% including the $\Sigma 3$ boundaries with a fraction of about 26%, about one half of that of the initial state, but larger than that after the impact at the velocity of 28.2 m s^{-1} . Visual observation indicates that the fraction of TBs within the $\Sigma 3$ boundaries is drastically reduced compared with the initial state (compare with Fig. 2a). The average grain size was about 3.7 μm , close to that for the initial state. In addition, the orientations within the grains are more homogeneous (compare Fig. 1d with Figs. 1b and 1c), meaning that the grains are less fragmented to tiny coherently diffracting domains, in accordance with X-ray line profile analysis discussed below. It is likely that dynamic recovery/recrystallization occurred here and led to a microstructure close to that of the initial, except for the crystallographic texture, as it will be shown later. Dynamic recrystallization during high strain rate deformation has been also reported in previous works [23,24]. The recrystallization process may have been assisted by the fast heat generation in the severe plastic deformation during impact test at a high strain rate (about 10^5 s^{-1} for 70.6 m s^{-1}). Actually, during high strain rate deformation, the fraction of plastic work, W_p that gets converted to heat in a unit volume during a supposedly adiabatic deformation process (assuming 90% of the work of the deformation was converted) is related to the temperature increase as [25–27]:

$$\Delta T = \frac{0.9W_p}{\rho C_p} \quad (2)$$

where ρ is the mass density and C_p is the specific heat at constant pressure. The ρ and C_p values for Ni are 8908 kg m^{-3} and 446 $\text{J kg}^{-1} \text{K}^{-1}$, respectively.

The mechanical behavior under dynamic loading has been discussed in earlier work [18]. These data predict temperature increase (ΔT) of about 15, 125 and 646 K at 10.9, 28.2 and 70.6 m s^{-1} impact velocities, respectively. Therefore, for the highest impact velocity, the homologous temperature of the sample immediately after the impact is $T/T_m \approx 0.55$, where T is the temperature after the impact ($300 \text{ K} + \Delta T = 946 \text{ K}$) and T_m is the melting temperature of Ni (1728 K). Rittel et al. [28] reported a ΔT increase of about 483 K in OFHC copper deformed over a wide range of strain rates which corresponds to a similar homologous temperature of the sample ($0.58 T_m$) as at the highest impact velocity in our study. A recrystallized microstructure was reported as a consequence of the straining process. Therefore, such a dynamic recrystallization effect is also expected here. It should be noticed that, the value of ΔT estimated

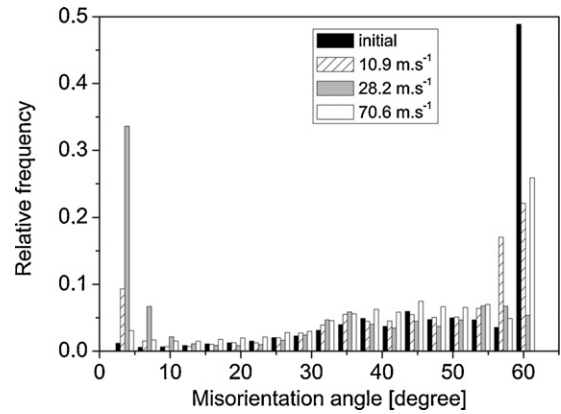


Fig. 3. The relative frequency of the misorientation across the boundary of the initial and impacted Ni samples.

here is larger compared to that (81 K) calculated for Cu processed by Equal Channel Angular Pressing (ECAP) at a strain of about 1 [29], or during severe plastic deformation of Al samples also processed by ECAP at the speed of 18 m s^{-1} , where the ΔT increase was between 30 and 70 K depending on the alloying element concentration in Al [30], which is close to the value observed here for the lowest velocity of 10.9 m s^{-1} .

Fig. 3 illustrates quantitatively the evolution of the misorientation across the grain boundaries for the samples studied here. In addition to the trends described above, it is observed that the increase of the amount of LAGBs occurs mainly at the expense of $\Sigma 3$ boundaries during impact tests, particularly for the sample impacted at 28.2 m s^{-1} . It is expected that the LAGBs were formed by the rearrangement of dislocations produced during impact test in order to reduce their strain energy.

3.2. X-ray line profile analysis

X-ray line profile analysis was carried out as a complement to the EBSD investigations. The experimental procedure was described in Section 2. As an example, the fitting in logarithmic intensity scale for the sample processed by impact test at 10.9 m s^{-1} is shown in Fig. 4a. The open circles and the solid line represent the measured data and the fitted curves, respectively. It should be noted that for the initial sample and for the specimen impacted at 70.6 m s^{-1} , the intensity distribution along the Debye–Scherrer rings is inhomogeneous and numerous sharp intensity spots are visible as it can be seen in Fig. 4b. These sharp peaks were as narrow as the instrumental broadening ($\Delta(2\theta) = 0.02^\circ$); therefore they were not evaluated for the microstructure. These sharp intensity spots are related to reflecting grains where the grain size is larger and the dislocation density is lower than the detection limits of X-ray line profile analysis for the experimental setup (800 nm and 10^{13} m^{-2} , respectively).

In the cases of the initial sample and that impacted at 70.6 m s^{-1} , only the broader and more homogeneous parts between the large intensity spots were evaluated by line profile analysis. As a consequence, the results obtained for these two samples characterize only a fraction of the whole microstructure. In the case of the samples impacted at 10.9 and 28.2 m s^{-1} , due to the small crystallite size and the large dislocation density, the Debye–Scherrer rings were relatively homogeneous therefore for these samples the microstructural parameters characterize the whole specimens. The mean crystallite size, the dislocation density (ρ_{dis}) and the twin fault probability (β) determined by X-ray line profile analysis are listed in Table 3.

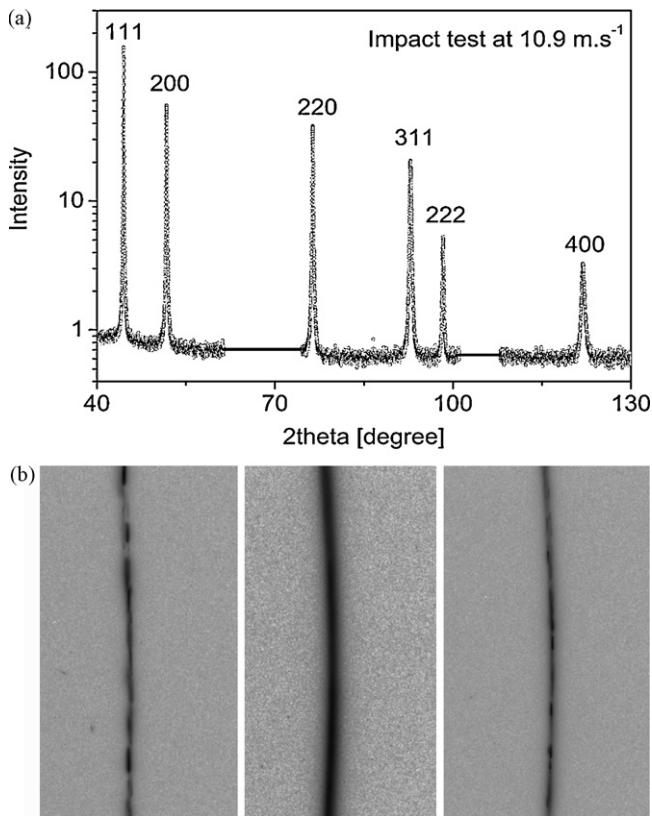


Fig. 4. (a) The fitting of the X-ray diffraction pattern for 10.9 m s^{-1} ; (b) diffraction rings for the (200) reflection corresponding to the initial state (left) and after impact at 10.9 m s^{-1} (middle) and at 70.6 m s^{-1} (right). The rings corresponding to initial state and after impact at 70 m s^{-1} exhibit clear spots, contrariwise to that obtained after impacting at 10 m s^{-1} .

It can be concluded from Table 3, that the impact test resulted in an increase of the dislocation density and a decrease of the crystallite size up to 28.2 m s^{-1} . The crystallite size measured by the present X-ray line profile analysis is smaller than the grain size obtained by EBSD. This phenomenon is usual in severely deformed metals [31] and it can be attributed to the fact that the crystallites are the domains in the microstructure which scatter X-rays coherently. As the coherency of X-rays breaks even if they are scattered from volumes having quite small misorientations ($1\text{--}2^\circ$), the crystallite size corresponds rather to the subgrain size in the severely deformed microstructures [32].

Table 3

Microstructure characteristics determined from X-ray line profile analysis, in terms of the mean crystallite size, the dislocation density (ρ_{dis}) and the twin fault probability (β). The latter quantity is defined as the relative fraction of twin boundaries among $\{111\}$ lattice planes.

Sample state	Crystallite size (nm)	ρ_{dis} (10^{14} m^{-2})	β (%)
Initial, fraction having broad X-ray peaks	149 ± 15	1.2 ± 0.2	0.0 ± 0.1
Initial + quasi-static compression	71 ± 8	10 ± 1	0.0 ± 0.1
$V = 10.9 \text{ m s}^{-1}$	113 ± 12	8 ± 1	0.0 ± 0.1
10.9 m s^{-1} + quasi-static compression	90 ± 10	9 ± 1	0.0 ± 0.1
$V = 28.2 \text{ m s}^{-1}$	64 ± 8	13 ± 1	0.0 ± 0.1
28.2 m s^{-1} + quasi-static compression	76 ± 8	15 ± 1	0.0 ± 0.1
$V = 70.6 \text{ m s}^{-1}$, fraction having broad X-ray peaks	420 ± 40	1.4 ± 0.2	0.7 ± 0.1

The crystallite size decreased while the grain size increased up to 28.2 m s^{-1} as observed by X-ray line profile analysis and EBSD, respectively. This apparent dichotomy can be explained by the activity of dislocations during impact test. The dislocations formed in plastic straining on the one hand destroy the $\Sigma 3$ boundaries [33,34] and on the other hand they are arranged into low energy configurations (e.g. into LAGBs). The former effect results in an increase of the mean grain size in EBSD experiments while the latter one reduces the size of coherently scattering domains (crystallites). In addition, in the EBSD analysis conducted here, the boundary misorientations lower than 2° were removed from the analysis.

At the same time, for the highest impact velocity (70.6 m s^{-1}), the crystallite size is larger while the dislocation density is smaller than for lower impact velocities, which indicates a dynamic recovery/recrystallization of the microstructure due to the fast deformation which is most probably also assisted by the temperature increment during impact test. This is in line with the discussion in the previous section. Indeed, the sharp intensity spots in the Debye–Scherrer rings are related to recrystallized grains while the broader sections between them correspond to recovered volumes. The characteristic parameters of the latter parts of the microstructure can also be found in Table 3 with the notation “fraction having broad peaks”. Of course, as these parameters characterize only a part of the microstructure, the mean crystallite size and the dislocation density for the whole sample are larger and smaller, respectively, than these values.

EBSD investigation allowed a quantitative assessment of the fraction of HAGBs which includes $\Sigma 3$ coincident site lattice (CSL) boundaries comprising TBs. As it can be seen in Table 3, X-ray line profile analysis allowed determining the twin probability, with a lowest detection limit of about 0.1%. This value corresponds to a twin boundary spacing of about 200 nm, therefore in the samples where the mean spacing between the twin boundaries is higher than this value, the line profile analysis cannot give the twin probability. Consequently, the zero value of the twin probability for the initial sample (see Table 3) is not in contradiction with the significant amount of TBs obtained by EBSD as the twin boundaries studied in EBSD have spacing larger than $1 \mu\text{m}$. However, for the sample impacted at 70.6 m s^{-1} , a significant value of twin probability (0.7%) was detected by X-ray line profile analysis in the volumes having broad diffraction peaks. This twin probability corresponds to an average TB spacing of about 30 nm. It is noted that EBSD analysis showed a marginal density of TBs at 70.6 m s^{-1} but this is not in contradiction with X-ray results as the latter method detected the twin probability inside the crystallites while the step size used in EBSD probably did not allow to measure twins with thickness lower than 100 nm. Moreover, only the volumes resulting in broad X-ray peaks could have been evaluated in the line profile analysis, while in the recrystallized fraction having narrow peaks the twin probability must be lower by orders of magnitude, therefore the average twin probability for the whole sample is most probably much lower than 0.7%. In addition, the average strain rate corresponding to the highest impact velocity of 70.6 m s^{-1} is about $2 \times 10^4 \text{ s}^{-1}$ which in the regime where thermally activated dislocation mechanisms are substituted by dislocation–drag effects [18,35]. Therefore, the expected reduced movement of partial dislocations in $\{111\}$ planes might limit the length of twins which may be a reason why they were not observed during EBSD investigations. This is in line with the work of Xiao et al. [36] who have also reported profuse mechanical twinning in a Cu–Zn alloy during dynamic plastic deformation at a strain rate of about 10^3 s^{-1} where the twin thickness was in the range of 10–20 nm, well below the detection limit of the EBSD investigation carried out here.

The viscous dislocation–drag effect mentioned above may explain the increase of the twin probability detected by X-ray line

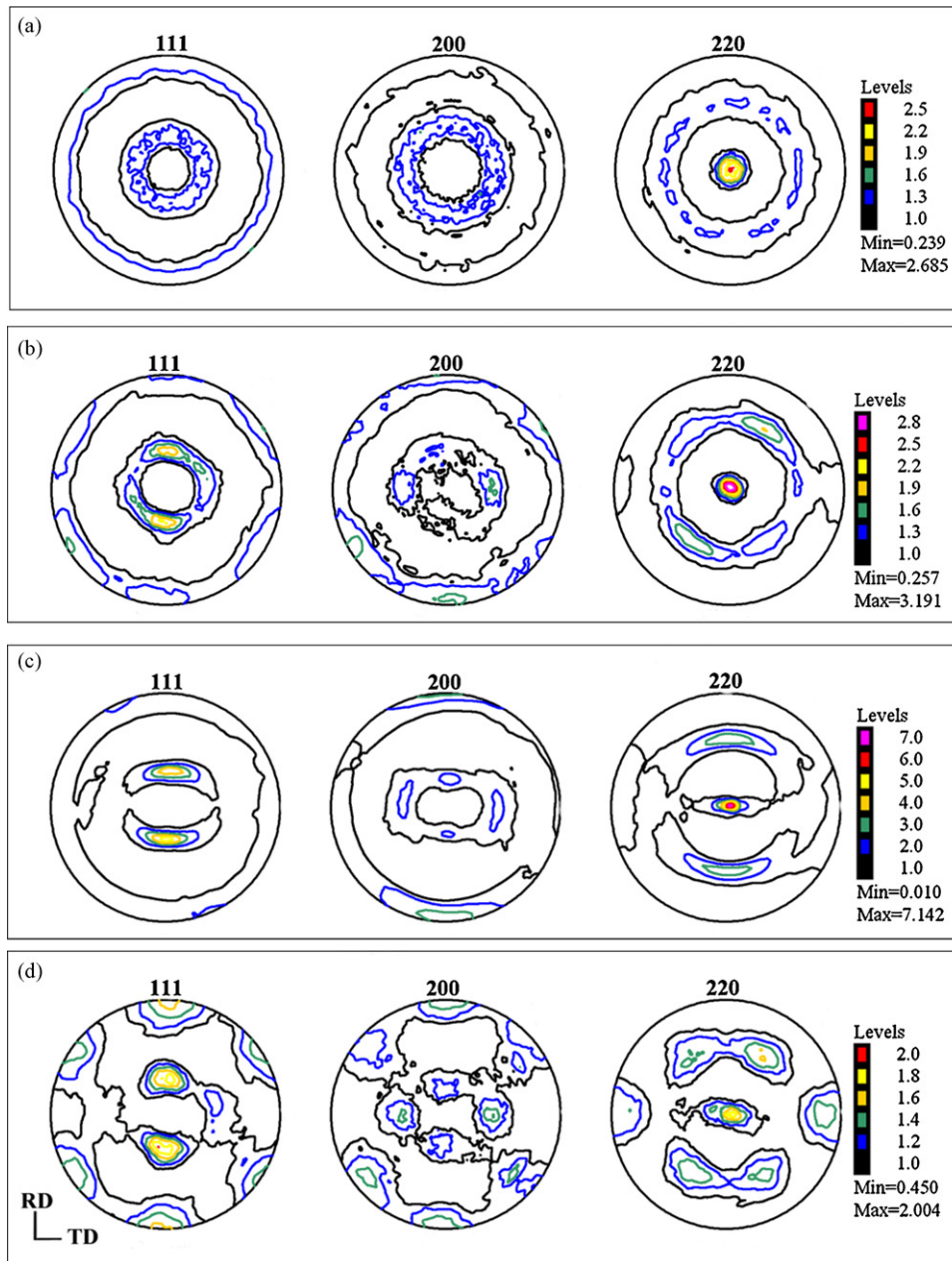


Fig. 5. Evolution of the crystallographic texture in terms of $\{111\}$, $\{200\}$ and $\{220\}$ pole figures in the (RD, TD) plane (see (d)) of the Ni samples. (a) Initial state; (b)–(d) after impact at 10.9, 28.2 and 70.6 m s^{-1} velocities, respectively.

profile analysis in the non-recrystallized volumes at 70.6 m s^{-1} . As shown in numerous studies [18,37,38], a sharp increase of the flow stress is usually observed within the viscous regime. Accordingly, if the local stresses exceed the critical stress required for twin nucleation, plasticity will continue by twinning. It has been also shown that at the highest strain rates associated with shocks, a transition occurred from plasticity controlled by dislocation or twinning defect movements to control by slip or twinning defect generations [39]. It should be also noted that the strain rate corresponding to the highest impact velocity applied here (70.6 m s^{-1}) falls in the regime ($1.5 \times 10^4 \text{ s}^{-1}$ to $2 \times 10^4 \text{ s}^{-1}$) where the phonon–drag effects are supposed to play a dominant role in dislocation generation. This may result in a significant increase of the dislocation density at very high strain rates, even for a strain as small as $\varepsilon=0.15$ as it was shown in Fig. 3 of Ref. [40]. The very high dislocation density developed at such a relatively small

strain value during the impact process at 70.6 m s^{-1} may also facilitate the dynamic recovery/recrystallization when the deformation proceeds.

3.3. Crystallographic texture investigations

Fig. 5 shows the recalculated pole figures of the Ni samples as a function of impact velocities. The results are quantitatively summarized in Table 4, including the volume fractions (VFs) of the main textures components. The VFs were extracted from the analysis of the orientation distribution functions (ODFs) (not shown here) as a function of the impact velocities. VFs were calculated by an integration method using Labotex software version 3.0 from LaboSoft s.c. The “Singly Counts in Overlapping Area” method was used to correct overlapping integration ranges between the different components [19].

Table 4

The volume fractions (VF) of major texture components extracted from the ODF analysis as a function of the impact velocities.

	Initial state	$V = 10.9 \text{ m s}^{-1}$	$V = 28.2 \text{ m s}^{-1}$	$V = 70.6 \text{ m s}^{-1}$
$\langle 110 \rangle$ Fiber	35.81%	30.46%	35.41%	–
$\{110\}\langle 100 \rangle$ Goss	–	4.70%	8.23%	7.25%
$\{110\}\langle 112 \rangle$ Brass	–	–	4.12%	3.08%
$\{123\}\langle 634 \rangle$ S	–	4.65%	6.71%	6.04%
$\{112\}\langle 111 \rangle$ Copper	–	4.80%	6.93%	7.60%
$\{110\}\langle 111 \rangle$	–	–	–	3.27%
$\{100\}\langle 011 \rangle$ D-Cube	–	–	–	4.10%
$\{100\}\langle 001 \rangle$ Cube	–	–	–	3.19%
$\{110\}\langle 233 \rangle$ P	–	–	–	4.34%
Rest of orientations	64.19%	55.38%	38.61%	61.14%

VFs were calculated by the integration method using Labotex software version 3.0 from LaboSoft s.c. The “Singlely Counts in Overlapping Area” method was used to correct overlapping integration ranges between different components [http://www.labosoft.com.pl].

The analysis highlights huge differences between the initial and the impacted states in terms of the major texture components:

- (i) For the initial state (Fig. 5a) a $\langle 110 \rangle$ fiber texture type ($\langle 110 \rangle$ crystallographic direction is normal to the impacted surface while there is a crystallographic isotropy in this plane) was found.
- (ii) After the impact at 10.9 m s^{-1} (Fig. 5b), the VF value of the $\langle 110 \rangle$ fiber component decreased while FCC cold rolled-type texture components (so-called Goss $\{110\}\langle 001 \rangle$, Brass $\{110\}\langle 1\bar{1}2 \rangle$, Copper $\{110\}\langle 1\bar{1}1 \rangle$, and S $\{123\}\langle 634 \rangle$) were developed.
- (iii) For the sample impacted at the velocity of 28.2 m s^{-1} (Fig. 5c), VF values of all these new components increased. In addition, the VF value of the fiber component was similar to that of the undeformed initial state.
- (iv) For the sample processed with the highest impact velocity of 70.6 m s^{-1} (Fig. 5d), the $\langle 110 \rangle$ fiber texture component disappeared, and beside the minor texture components appeared at 28.2 m s^{-1} , new components are detected that usually develop during recrystallization processes. These are the Cube $\{100\}\langle 001 \rangle$, deviated Cube D-Cube $\{100\}\langle 011 \rangle$ and P $\{110\}\langle 233 \rangle$. The texture analysis strongly supports the idea of a recrystallization process occurring for Ni samples in the course of straining at the highest impact velocity.

3.4. Nanohardness investigations

Nanoindentation tests were carried out to make sure of the occurrence of recovery/recrystallization during impact test at the highest velocity. The resulting nanohardness distributions for the initial specimen and those processed by impact test at different velocities are shown in Fig. 6a.

The mean nanohardness of the initial sample is 2.7 GPa which increases to 3.7 and 5.1 GPa due to impact tests at velocities of 10.9 and 28.2 m s^{-1} , respectively, which can be attributed to an increase of the dislocation density. After the impact test at 70.6 m s^{-1} the mean nanohardness decreased to the same value (2.7 GPa) as in the initial case. This can be explained only by the occurrence of recovery/recrystallization during impact test as discussed above (see Section 3.2).

As already reported elsewhere, it should be noted that:

- (i) The hardness calculated by Eq. (1) is generally different from the value obtained from the indent size determined by microscopy methods owing to the distortion of the shape of residual indentation pattern after removing the tip from the surface of probe material [41].

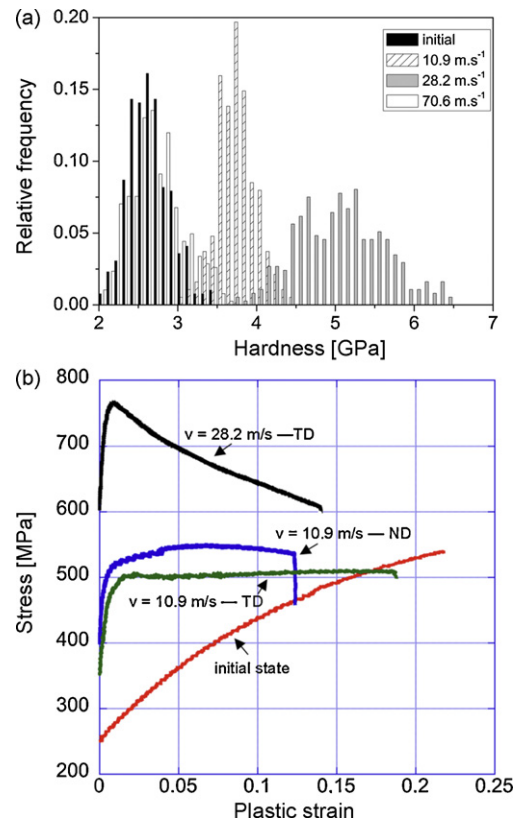


Fig. 6. (a) Nanohardness distribution as function of the impact velocity for the different impacted Ni samples. The nanohardness distribution for the initial state is also shown. (b) Stress–strain plots obtained by quasi-static compression tests at room temperature for the initial and impacted Ni samples. ND or TD refers to a compression axis parallel or perpendicular to the impact direction.

- (ii) Generally, the hardness measurement results in an additional 8% plastic deformation [42], i.e. the hardness measured at relatively high load ($2 \text{ N} \leq P_{\text{max}}$) is related to the flow stress corresponds to 8% strain.
- (iii) Nanohardness value cannot be used directly for the determination of the flow stress because of the so-called indentation size effect. This means that the hardness of a material increases with the decrease of indentation size and the flow stress can be determined only from the macrohardness value.

3.5. Quasi-static compression tests at room temperature

Fig. 6b shows the true stress–true plastic strain plots for the initial sample and the specimens impacted at 10.9 and 28.2 m s^{-1} obtained in quasi-static compression tests at room temperature and at a strain rate of 10^{-4} s^{-1} . Due to the very small height of the sample processed at 70.6 m s^{-1} , that sample was not studied by compression. The following observations can be made from the compression tests:

- (i) The initial sample showed a classical behavior with a positive strain-hardening rate due to dislocations–dislocation and dislocation–boundary interactions. As shown in Table 3, after compression test the dislocation density and the crystallite size are much higher and lower, respectively, than the values characteristic for the undeformed initial sample.
- (ii) For the sample impacted at the velocity of 10.9 m s^{-1} , the stress–strain behavior depends slightly on the direction of the stress in quasi-static compression test. The sample subjected to a compressive stress parallel to the impact direction (ND

sample) exhibits slightly higher yield strength than the sample with the compression axis perpendicular to the impact direction (TD sample). Similar phenomenon was also reported by Abdul-Latif et al. [43] in the case of pure Al crushed at a velocity of about 10 m s^{-1} . This behavior can be explained by the $\langle 110 \rangle$ texture in the impact direction (see Section 3.3), as the Taylor factor in this direction is higher than for the random crystallographic orientation by about 20% [44]. The hardening rate of sample ND was much lower than that of the initial sample. This observation is in line with the results obtained by X-ray line profile analysis on the ND sample (see Table 3), as the decrease of the crystallite size as well as the increase of the dislocation density are very remote during compression test.

- (iii) Because of the thickness reduction, the sample impacted at 28.2 m s^{-1} was tested only in the TD direction. The stress–strain curve exhibits a softening (a negative strain hardening rate) that is observed just after the maximum compression stress was reached. Both the yield strength and the flow stress are far higher than for all the other cases studied here. This observation is in line with the highest measured dislocation density in the sample impacted at 28.2 m s^{-1} among the specimens investigated in this study (see Table 3). The microstructure might be already saturated with dislocations, therefore it is presumed that the softening is caused by an early strain localization due to the high flow stress. It is also noted that if microcracks formed during high-speed impact test, they may also contribute to softening.

4. Conclusions

High purity nickel samples deformed dynamically in compression using a direct impact Hopkinson pressure bar at impact velocities of 10.9, 28.2 and 70.6 m s^{-1} have been investigated. A complete microstructure characterization has been undertaken combining EBSD, crystallographic texture measurement and X-ray line profile analysis. The local and the macroscopic mechanical behaviors were studied by nanoindentation and quasi-static compression test at room temperature, respectively. It was observed that:

- (i) Up to a velocity of 28.2 m s^{-1} , the dislocation density in the impacted samples increased which was accompanied by the reduction of the fraction of $\Sigma 3$ CSL type boundaries from 50 to 7% indicating that the main deformation mechanism was the motion of dislocation. The increase of the dislocation density yielded an increase of both nanohardness and compressive flow stress. The decrease of the amount of $\Sigma 3$ CSL type boundaries, that initially divide grains into smaller areas, caused an apparent increase of the mean grain size measured by EBSD.
- (ii) For the velocity of 70.6 m s^{-1} , it was observed that the microstructure resembled to that of the initial state in all characteristics, except for the crystallographic texture. EBSD investigations showed that the fraction of $\Sigma 3$ CSL type boundaries increased back to 26%. It was also found that the dislocation density was similar as the value measured before the impact test which was about one order of magnitude smaller than the value obtained after impact at 28.2 m s^{-1} . The

nanohardness was also the same as in the initial state. These features were ascribed to dynamic recovery/recrystallization processes taking place during the impact test most probably due to the increase of the homologous temperature to about 0.55. This conclusion was supported by crystallographic texture analysis showing the formation of recrystallization texture components such as Cube $\{100\}\langle 00 \rangle$, deviated Cube D-Cube $\{100\}\langle 011 \rangle$ and P $\{110\}\langle 233 \rangle$.

Acknowledgements

The authors are obliged to Mr. P. Szommer for processing nanohardness measurements. This work was supported in part by the Hungarian Scientific Research Fund, OTKA, Grant No. K 81360.

References

- [1] T. Watanabe, Res. Mech. 11 (1984) 47.
- [2] V. Randle, Acta Mater. 47 (1999) 4147.
- [3] S.H. Kim, U. Erb, K.T. Aust, G. Palumbo, Scr. Mater. 44 (2001) 835.
- [4] P. Lin, G. Palumbo, U. Erb, K.T. Aust, Scr. Metall. Mater. 33 (1995) 1387.
- [5] P.G. Sanders, C.J. Youngdahl, J.R. Weertman, Mater. Sci. Eng. A 234–236 (1997) 77.
- [6] S. Billard, J.P. Fondère, B. Bacroix, G.F. Dirras, Acta Mater. 54 (2006) 411.
- [7] W.Q. Cao, G.F. Dirras, M. Benyoucef, B. Bacroix, Mater. Sci. Eng. A 462 (2007) 100.
- [8] N. Tsuji, Y. Ito, Y. Saito, Y. Minamino, Scr. Mater. 47 (2002) 893.
- [9] R.Z. Valiev, I.V. Alexandrov, Y.T. Zhu, T.C. Lowe, J. Mater. Res. 17 (2002) 5.
- [10] M. Dao, L. Lu, Y.F. Shen, S. Suresh, Acta Mater. 54 (2006) 5421.
- [11] L. Lu, R. Schwaiger, Z.W. Shan, M. Dao, K. Lu, S. Suresh, Acta Mater. 53 (2005) 2169.
- [12] H.S. Cho, K.J. Hemker, K. Lian, J. Goettter, G. Dirras, Sens. Actuators A 103 (2003) 59.
- [13] J. Gubicza, H.-Q. Bui, F. Fellah, G.F. Dirras, J. Mater. Res. 24 (2009) 217.
- [14] G. Dirras, S. Bouvier, J. Gubicza, B. Hasni, T. Szilágyi, Mater. Sci. Eng. A 526 (2009) 201.
- [15] U.F. Kocks, H. Mecking, Prog. Mater. Sci. 48 (2003) 171.
- [16] T.E. Buchheit, D.A. LaVan, J.R. Michael, S.D. Leith, Metall. Mater. Trans. 33A (2002) 539.
- [17] L.E. Murr, E.A. Trillo, S. Papu, C. Kennedy, J. Mater. Sci. 37 (2002) 3337.
- [18] H. Couque, R. Boulanger, in: F. Gálves, V. Sanchez-Galves (Eds.), Proceedings of the 23rd International Symposium on Ballistics, Tarragona, 2007, pp. 255–262.
- [19] <http://www.labosoft.com.pl>.
- [20] G. Ribárik, J. Gubicza, T. Ungár, Mater. Sci. Eng. A 387–389 (2004) 343.
- [21] L. Balogh, G. Ribárik, T. Ungár, J. Appl. Phys. 100 (2006) 023512.
- [22] F. Fröhlich, P. Grau, W. Grellmann, Phys. Stat. Sol. 42 (1977) 79.
- [23] L.E. Murr, E.V. Esquivel, J. Mater. Sci. 39 (2004) 1153.
- [24] L.E. Murr, C. Pizana, Metall. Mater. Trans. A 38A (2007) 2611.
- [25] J.J. Mason, A.J. Rosakis, G. Ravichandran, Mech. Mater. 17 (1994) 135.
- [26] S. Nemat-Nasser, L. Ni, T. Okinaka, Mech. Mater. 30 (1998) 325.
- [27] D. Rittel, Mech. Mater. 31 (1999) 131.
- [28] G. Rittel, S. Ravichandran, S. Lee, Mech. Mater. 34 (2002) 627.
- [29] W.J. Kim, K.E. Lee, S.-H. Choi, Mater. Sci. Eng. A 506 (2009) 71.
- [30] D. Yamaguchi, Z. Horita, M. Nemoto, T.G. Langdon, Scr. Mater. 41 (1999) 791.
- [31] T. Ungár, J. Gubicza, Z. Kristallogr. 222 (2007) 114–128.
- [32] T. Ungár, G. Tichy, J. Gubicza, R.J. Hellmig, Powder Diffract. 20 (2005) 366.
- [33] P. Müllner, C. Solenthaler, Mater. Sci. Eng. A 230 (1997) 107.
- [34] L. Lu, Y. Shen, X. Chen, L. Qian, K. Lu, Science 304 (2004) 422.
- [35] P.S. Follansbee, U.F. Kocks, Acta Metall. 1 (1988) 81.
- [36] G.H. Xiao, N.R. Tao, K. Lu, Scr. Mater. 59 (2008) 975.
- [37] H. Zhang, K.T. Ramesh, E.S.C. Chin, Mater. Sci. Eng. A 384 (2004) 26.
- [38] E. El-Magd, M. Abouridouane, Int. J. Impact Eng. 32 (2006) 741.
- [39] R.W. Armstrong, S.M. Walley, Int. Mater. Rev. 53 (2008) 105.
- [40] M. Huang, P.E.J. Rivera-Díaz-del-Castillo, O. Bouaziz, S. van der Zwaag, Mech. Mater. 41 (2009) 982.
- [41] W.C. Oliver, G.M. Pharr, J. Mater. Res. 7 (1992) 1564.
- [42] D. Tabor, The Hardness of Metals, Clarendon Press, Oxford, 1951.
- [43] A. Abdul-Latif, G.F. Dirras, S. Ramtani, A. Hocini, Int. J. Mech. Sci. 51 (2009) 797.
- [44] B. Clausen, T. Lorentzen, T. Leffers, Acta Mater. 46 (1998) 3087.